Tracing Ammonia Emission Sources in California's Salton Sea Region: Insights from Airborne Longwave-Infrared Hyperspectral Imaging and Ground Monitoring

Sina Hasheminassab[1*], David M. Tratt[2], Olga V. Kalashnikova[1], Clement S. Chang[2], Morad Alvarez[2], Kerry N. Buckland[2], Michael J. ~~Garay~~[+]Garay[2], Francesca M. Hopkins[3], Eric R. Keim[2], Le Kuai[1], Yaning Miao[3], Payam Pakbin[4], William C. Porter[3], Mohammad H. Sowlat[4]

[1] Jet Propulsion Laboratory, California Institute of Technology, Pasadena, CA 91011, USA
[2] The Aerospace Corporation, Los Angeles, CA 90009, USA
[3] University of California, Riverside, CA 92521, USA
[4] South Coast Air Quality Management District, Diamond Bar, CA 91765, USA

* Correspondence to: Sina Hasheminassab (sina.hasheminassab@jpl.nasa.gov)

Abstract

Ammonia (NH_3) plays an important role in atmospheric chemistry and air quality, but its emissions remain poorly constrained due to its short atmospheric lifetime, high spatial heterogeneity, and limited coverage of existing monitoring resources. This study integrates airborne longwave-infrared (LWIR) hyperspectral imaging at ~2 m spatial resolution with ground-based stationary and mobile in-situ measurements to map and characterize NH_3 emissions in two regions near the Salton Sea in Southern California: Mecca in the northwest and Imperial in the southeast. Airborne surveys conducted in March and September 2023 with a wide-swath LWIR spectral imager revealed pronounced spatial and seasonal variability. Average NH_3 levels in Imperial were 2.5 to 8 times higher than those in Mecca, linked primarily to large, concentrated animal feeding operations (CAFOs), geothermal power plants, fumaroles, and intensive agricultural activities. Ground-based mobile monitoring corroborated these findings, showing elevated NH_3 levels near these sources and especially high NH_3 concentrations downwind of CAFOs with large cattle populations. The results underscore the utility of airborne LWIR hyperspectral imaging in detecting and mapping NH_3 at hyperlocal scales, including sources absent from existing inventories. They further highlight the need for routine airborne campaigns and the development of next-generation satellite missions with higher spatial resolution to achieve comprehensive, large-area monitoring. These findings inform air quality management strategies and emphasize the importance of improving emission inventories for effective mitigation of NH_3-driven air pollution.

1. Introduction

Ammonia (NH_3) is a critical component of the atmospheric nitrogen cycle and an important precursor for the formation of fine particulate matter ($PM_{2.5}$) (Tang et al., 2025; Wyer et al., 2022a). It is primarily emitted from agricultural activities, particularly livestock waste and the application of fertilizers, but also from combustion sources such as vehicles and biomass burning (Beaudor et al., 2025; Vira et al., 2022; Zeng et al., 2018). As the

39   primary form of reactive nitrogen in the environment, it plays an important role in nitrogen deposition,

40   eutrophication, and acidification processes (Li et al., 2025; Zhang et al., 2012). Additionally, atmospheric NH_3 reacts

41   with acidic compounds like nitric and sulfuric acids to form ammonium salts, contributing significantly to secondary

42    $PM_{2.5}$, leading to various adverse health outcomes (Wyer et al., 2022b).

43   Recent studies have reported increasing trends in atmospheric NH_3 levels at global and regional scales, driven

44   largely by agricultural activities, industrial processes, and changing climatic conditions (Kuttippurath et al., 2024;

45   Ma et al., 2025; Van Damme et al., 2021; Wang et al., 2023; Yu et al., 2018). For example, Van Damme et al. (2021)

46   reported a 12.8 % global increase between 2008 and 2021 based on the Infrared Atmospheric Sounding

47   Interferometer (IASI) satellite measurements. During the same period, also using IASI data, Wang et al. (2023)

48   observed a 6.8 % annual increase in NH_3 concentrations across the contiguous U.S., with hotspots concentrated in

49   agricultural regions. Also, during the 2020 COVID-19 lockdown, Kuttippurath et al. (2024) found that unlike most

50   pollutants which declined, NH_3 levels rose, largely due to sustained or increased agricultural activity. Consequently,

51   regulatory bodies such as the European Parliament and air quality agencies in California are recognizing NH_3 as an

52   emerging pollutant of concern (European Commission, 2022; South Coast AQMD, 2024). Furthermore, the recent

53   tightening of the U.S. Environmental Protection Agency's (EPA) National Ambient Air Quality Standards (NAAQS)

54   for annual average $PM_{2.5}$ to 9 µg m^{-3} has drawn increasing attention to NH_3, particularly in non-attainment areas, to

55   better characterize its sources and contribution to secondary $PM_{2.5}$ (Reconsideration of the National Ambient Air

56   Quality Standards for Particulate Matter, 88 Fed. Reg. 5558 | Casetext, 2025). However, unlike other key gas-phase

57   precursors of $PM_{2.5}$ such as NO_2 and SO_2, which are regulated as criteria pollutants in the U.S. and are widely

58   monitored, the scarce monitoring of NH_3 and uncertainties in emissions inventory hinder accurate assessments of its

59   contribution to secondary $PM_{2.5}$ formation.

60   Despite its importance, measuring and characterizing NH_3 emissions are challenging due in part to its short

61   atmospheric lifetime, high spatial heterogeneity, reactivity, and solubility (Nair and Yu, 2020). Established ground-

62   based monitoring networks, such as the Ammonia Monitoring Network (AMoN) in the U.S., provide high-quality

63   data but are spatially sparse and temporally limited to biweekly measurements (Felix et al., 2017). Existing satellite

64   instruments capable of detecting NH_3 (e.g., CrIS, IASI, AIRS) offer broader spatial coverage, but generally at coarse

65   spatial resolutions (15-50 km) inadequate for the identification of local-scale emission sources (Dammers et al.,

66   2019; Shephard et al., 2020; Warner et al., 2016). Due to these challenges, current chemical transport model

67   emission inventories often fail to adequately represent major NH_3 sources, leading to significant underestimation of

68   their contributions (Burns et al., 2023).

69   The longwave-infrared (LWIR) hyperspectral imaging technique is highly effective at identifying diagnostic spectral

70   features of various environmentally important gases, with a particularly strong sensitivity to NH_3 (Kuai et al., 2019;

71   Leifer et al., 2017). Airborne deployment of this technique enables wide-area, high-resolution mapping of NH_3

72   emissions. Airborne instruments such as The Aerospace Corporation's Mako imager and JPL's Hyperspectral

73   Thermal Emission Spectrometer (HyTES) have demonstrated the capability to detect and quantify NH_3 with spatial

74   resolutions ranging from 1 to 30 m, depending on flight altitude (Hall et al., 2011; Hulley et al., 2016; Kuai et al.,

75   2019; Tratt et al., 2013). This high-resolution capability is particularly important in complex regions where multiple

76   emission sources coexist.

77   The Salton Sea region in Southern California represents an important NH_3 hotspot with unique air quality challenges

78   and opportunities for study. Intensive agricultural activities, including large-scale concentrated animal feeding

79   operations (CAFOs) and extensive fertilizer application, as well as industrial and natural geothermal emissions,

80   contribute to its high NH_3 levels. The Imperial Valley, located in the southern part of the Salton Sea, has one of the

81   highest densities of CAFOs in California and ranks among the top ten NH_3 hotspots in the U.S. (Wang et al., 2023).

82   Despite its significance, NH_3 sources in this region have not been extensively monitored or thoroughly

83   characterized.

84   This study aims to address these gaps by integrating airborne LWIR hyperspectral imaging with ground-based

85   stationary and mobile in-situ monitoring to map and characterize NH_3 emissions in the Salton Sea region. Using this

86   multi-platform approach, we identify major NH_3 sources, including previously undocumented or underrepresented

87   ones, and assess their spatial and temporal variability in these complex environments. The findings provide a

88   foundation for improving NH_3 inventories and underscore the necessity for routine airborne measurements and

89   development of satellite missions with higher spatial resolution to resolve persistent data gaps in understanding

90   NH_3's contribution to atmospheric chemistry and air quality. This demonstration is timely, given the growing global

91   demand for better NH_3 monitoring at scale.

92   **2. Methodology**

93   **2.1. Overview**

94   The study focused on the Salton Sea region in Southern California, selected for its diverse and significant NH_3

95   emission sources and unique environmental characteristics. Measurements included airborne remote sensing and

96   ground-based in-situ monitoring, both mobile and stationary. Figure 1 illustrates the study areas, the footprints of

97   airborne remote sensing measurements, the routes covered by the mobile platform, and the location of the air

98   monitoring site utilized in this research. The following sections detail each component of the study.
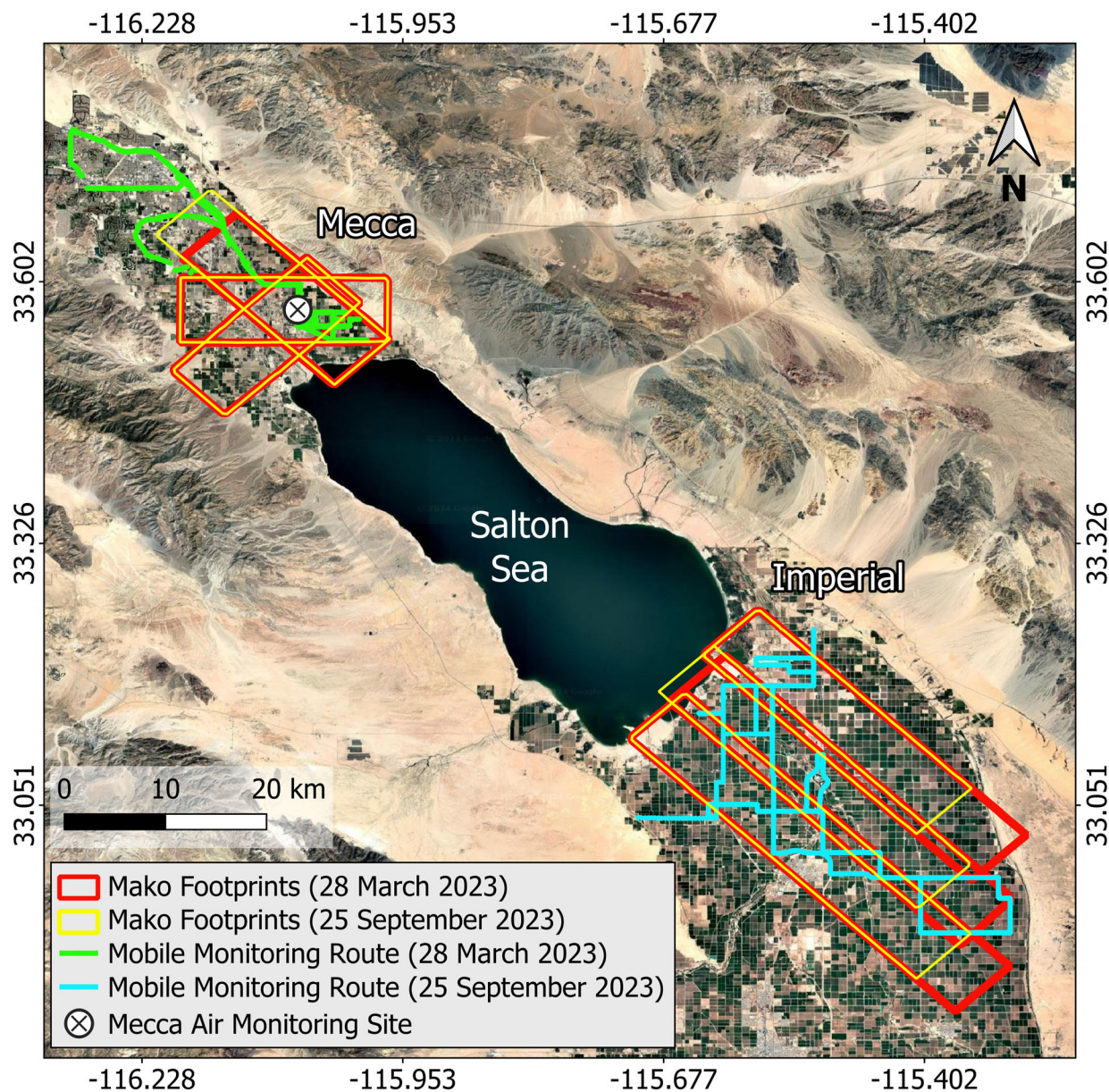
Figure 1. Map of study areas around the Salton Sea. The northwestern area is denoted as "Mecca," and the southeastern area as "Imperial," and they are referred to as such throughout the paper. ~~Map data~~**Base imagery ©2025 Google.**

2.2. Study Areas

The study areas encompass the northwest and southeast regions of the Salton Sea, hereafter referred to as Mecca and Imperial, respectively (Figure 1). Both areas are predominantly rural and surrounded by extensive agricultural lands. Mecca is known for cultivating high-value crops such as dates, citrus fruits, and vegetables, while Imperial is characterized by large-scale agricultural production, with a focus on crops including alfalfa, grains, and vegetables. Additionally, Imperial has a high concentration of CAFOs and several geothermal power plants (GPPs). Both regions face severe air pollution challenges, including agricultural emissions and windblown dust from surrounding desert regions as well as from the increasingly exposed dried lakebed surfaces (Bi et al., 2020; Frie et al., 2019;

110   Johnston et al., 2019; Lieb et al., 2024). Previous studies have reported a high prevalence of health issues related to

111   air pollution in this area, particularly impacting cardiovascular and respiratory systems (Farzan et al., 2019; Johnston

112   et al., 2024; Jones and Fleck, 2020; Miao et al., 2025). Both regions are designated as nonattainment for 8-hour

113   ozone and 24-hour PM_{10} standards, and Imperial is additionally nonattainment for annual $PM_{2.5}$ (Current

114   Nonattainment Counties for All Criteria Pollutants, 2025). Moreover, according to the California Office of

115   Environmental Health Hazard Assessment (OEHHA), these regions rank among the communities with the highest

116   pollution burdens and socioeconomic disadvantages in California and are therefore classified as environmental

117   justice communities.

118   **2.3. Airborne Measurements**

119   The airborne component of the study utilized The Aerospace Corporation's Mako imager, mounted on a Twin Otter

120   aircraft. Mako is a 3-axis stabilized whiskbroom imager spanning the LWIR spectral region (specifically 7.6-13.2

121   μm) in 128 contiguous channels capable of detecting and quantifying multiple gas species. The performance and

122   operating specifications of Mako have been detailed elsewhere (Buckland et al., 2017; Hall et al., 2016). For this

123   study, flights were conducted at an altitude of approximately 3,750 m above ground level (AGL), with a 7.5-

124   kilometer swath and a nominal ground sample distance (GSD) of 2.1 m. Flight measurements were conducted on

125   two different days in 2023, during distinct seasons: March 28th and September 25th. Figure 2 presents the airborne

126   data acquisition times for each day and region. On March 28th, measurements began over Mecca at approximately

127   10:37 AM PDT and continued until 11:08 AM PDT, followed by acquisitions in the Imperial region from 11:24 AM

128   to 12:12 PM PDT. On the return to base, another measurement was conducted over the SE-to-NW flight line over

129   Mecca (see Figure 4) between 12:40 PM and 12:46 PM PDT. Drawing from the experience gained during the March

130   campaign, the September flights aimed to further differentiate morning and afternoon measurements. Thus, on

131   September 25th, flight measurements commenced earlier, starting over Mecca at 9:35 AM PDT and continuing until

132   10:10 AM PDT. Data acquisition in the Imperial region was then conducted from 10:27 AM to 11:12 AM PDT. A

133   second round of measurements, over the same flightlines, was performed in the afternoon, with acquisitions over

134   Mecca between 3:06 PM and 3:39 PM PDT and over Imperial from 3:53 PM to 4:37 PM PDT. The flight paths were

135   identical on both days, with the exception of a northwestern extension of one flight line over Mecca and slightly

136   shorter flight lines over Imperial on September 25th, as shown in Figure 1. The extension over Mecca was intended

137   to capture the source of a plume attributable to a waste recycling facility that had been partially detected during the

138   March flights. More details about the emissions from this facility are provided in the results section. The shortened

139   flight lines in September were to avoid approaching restricted airspace that was encountered during the March

140   flights.

141
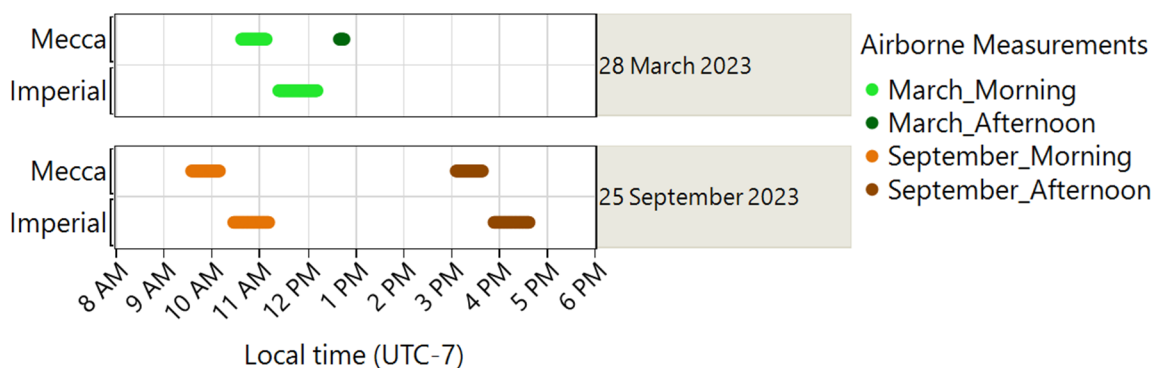
Figure 2. Timing of airborne measurements over the Mecca and Imperial study areas on March 28 and September 25, 2023. The time periods defined in the legend are used throughout the paper to distinguish measurement sessions.

During the September campaign, an additional series of airborne measurements in multi-scan (movie) mode was conducted over nine pre-determined sources, including GPPs, fumaroles, CAFOs, and a waste recycling facility. These measurements, collected at a nominal frame rate of 0.6 Hz during both morning and afternoon flight sessions, captured short-term temporal variations in NH_3 emissions from these sources. The data will be used to estimate emission fluxes from these sources, which will be the subject of a separate publication from this study.

2.4. NH₃ Retrieval

Details of the NH_3 retrieval methodology from Mako are described in Hall et al. (2025) and Tratt et al. (2025). Briefly, NH_3 column densities were retrieved using a custom Scene-based Algorithm for Gas Estimation (SAGE), which employs a nonlinear radiative transfer model and auxiliary data to estimate gas concentrations along the atmospheric path, reported in units of ppm-m (parts per million-meter). To evaluate the confidence of each retrieval, SAGE calculates a t-statistic that constitutes a measure of the retrieval signal-to-noise ratio. The algorithm also outputs fit residuals and the thermal contrast (ΔT), defined as the temperature difference between the near-surface air parcel and the underlying surface, for each pixel. In this study, pixels were thresholded using a t-statistic of ≥ 3.0 and $|\Delta T| \geq 2.0$ °C to eliminate high-uncertainty NH_3 abundance estimates. It should be noted that in all NH_3 column density maps in this paper, null pixels that did not meet the t-statistic and ΔT thresholds are rendered transparent to expose the underlying imagery.

The retrievals in this study were also validated against ground-based in-situ NH_3 measurements by incorporating air temperature and planetary boundary layer height (PBLH) fields from NOAA's High-Resolution Rapid Refresh (HRRR) model and Gaussian plume modeling to characterize atmospheric conditions and plume dynamics. The minimum detectable concentration (MDC) of ground-level NH_3 depends on thermal contrast and boundary layer height, and ranged from 3 to 33 ppbv over Mecca in September under varying atmospheric conditions. Validation against ground-based in situ measurements showed good agreement, with differences ranging from 16% to 37% under stable and well-mixed conditions. Detailed descriptions of the retrieval process, detection sensitivity, and validation results for the airborne component of this study are provided in Tratt et al. (2025).

2.5. Ground-Based In-Situ Stationary Monitoring

Continuous 1-minute NH_3 monitoring was conducted using a Picarro G2301 analyzer at the South Coast Air Quality Management District (South Coast AQMD) Mecca air monitoring site (AMS) (Figure 1). Routine quality assurance procedures, including monthly zero and span checks, were conducted by South Coast AQMD. Unfortunately, the instrument was non-operational for the entire month of March 2023, concurrent with the first day of airborne measurements. However, it was operational before and after March 2023, allowing the assessment of NH_3 levels on the second airborne measurement day in September and evaluation of its temporal trends throughout 2023.

2.6. Ground-Based In-Situ Mobile Monitoring

The mobile monitoring was conducted using a mobile platform developed and operated by the University of California, Riverside. This mobile platform was equipped with advanced instrumentation to continuously measure geolocated atmospheric NH_3 levels along roadways. The primary sensor was a Picarro G2123 cavity ring-down spectrometer, measuring NH_3 concentrations every ~3 s with a precision of 500 ppt, sampling ambient air through a ¼" Teflon line at a rate of 1.7 dm^3 min^{-1} from an inlet positioned 3 m AGL. GPS data, recorded every second by a roof-mounted Garmin GPS 16X receiver, provided precise geographical coordinates.

Mobile monitoring was conducted concurrently with the airborne measurements, with the routes shown in Figure 1. On March 28th, during the first airborne campaign and in the absence of stationary monitoring at the Mecca AMS, the mobile platform focused on the Mecca region. On September 25th, during the second airborne campaign, mobile monitoring covered the Imperial region.

2.7. Meteorology

Meteorological data, including temperature, wind speed, and direction at 10 m AGL, and PBLH, corresponding to the study areas and flight measurement periods, were retrieved from NOAA's HRRR model output using the Herbie Python package (https://zenodo.org/records/13329302; accessed 4 January 2025). Figures S1 and S2 provide a summary of these meteorological parameters across the study regions during each flight measurement session.

Temperatures were generally comparable between Mecca and Imperial, ranging from approximately 20°C in March to 31°C during the September morning flights, and rising further to 37°C in September afternoon. During the March campaign, PBLH values ranged from 730 to 937 m across both regions. During the September morning flights, which began earlier in the day, PBLH values were lower, around 340 m in Mecca and 554 m in Imperial. However, by the afternoon, PBLH significantly increased to 1,821 m in Mecca and 1,592 m in Imperial.

The wind direction/speed varied largely across the study area and over time. During the March morning flights, both Mecca and Imperial experienced light winds ranging from 0 to 2 m s^{-1}, with Mecca dominated by southerly winds and Imperial by northwesterly winds. By the afternoon, wind speeds in Mecca increased substantially, exceeding 4 m s^{-1}. In September morning, winds were predominantly northwesterly in both regions, with Mecca exhibiting stronger winds averaging 1.6 m s^{-1} compared to 0.95 m s^{-1} in Imperial. By the afternoon, wind speeds increased in

202 both areas; while Imperial's winds remained primarily northwesterly with an average speed of 1.5 m s^{-1}, Mecca
203 experienced a notable shift in wind direction to southeasterly, with an average speed of 3.1 m s^{-1}.

2.8. Spatial Data of Potential NH$_3$ Emitters

205 The study area around the Salton Sea is home to several notable NH$_3$ emission sources, including fumaroles,
206 CAFOs, GPPs, and waste recycling facilities. To attribute the observed NH$_3$ hotspots to these known emitters—and
207 potentially identify any previously unknown or unreported sources—geospatial data on their locations and attributes
208 were compiled from various sources. Data on GPPs, including their locations and generating capacities, were
209 obtained from the California State Geoportal (https://gis.data.ca.gov, accessed January 4, 2025). Information on
210 CAFOs, such as facility locations and cattle populations, was sourced from the California Air Resources Board's
211 (CARB) California Dairy & Livestock Database (CADD) (https://ww2.arb.ca.gov/resources/documents/california-
212 dairy-livestock-database-cadd, accessed January 4, 2025). Information about waste recycling facilities was obtained
213 from EPA's Toxic Release Inventory (TRI) (https://www.epa.gov/toxics-release-inventory-tri-program/tri-toolbox,
214 accessed January 4, 2025). Additionally, the locations of known fumaroles along the southern shore of the Salton
215 Sea were gathered from previous studies conducted in the region (Adams et al., 2017; Tratt et al., 2011, 2016).
216 Nearly all of the abovementioned sources were located in the Imperial study area, with the exception of a waste
217 recycling facility located in the Mecca region.

218 Figure S3 shows the total cattle population at CAFO facilities within the Imperial study area in 2022. Among these,
219 CAFO 1 stands out with the largest cattle population, approximately 150,000, far exceeding the numbers at other
220 CAFOs in the study area. In fact, according to CADD, CAFO 1 has the largest cattle population of any CAFO in
221 California (data not shown). Additionally, CAFOs 2 and 9 rank seventh and eighth statewide, respectively. Figure S4
222 shows the generating capacities of GPPs in the Imperial region, with GPPs 9, 3, 4, 5, and 11 having the highest
223 capacities, ranging from 50 to 55 MW.

2.9. Data Analysis

225 Data analyses, visualizations, and mapping were performed using R, QGIS, and SAS JMP. To investigate the source
226 directionality of NH$_3$ at the Mecca AMS, bivariate directional analyses were conducted using the openair package in
227 R.

3. Results

3.1. Airborne Measurements

230 Figure 3 shows the average NH$_3$ column density across both study areas during each airborne measurement session.
231 As shown, average NH$_3$ levels were significantly higher in Imperial compared to Mecca, with respective factors of
232 approximately 8 and 2.5 during the March and September campaigns. Seasonally, Mecca NH$_3$ levels were about 3.5
233 times higher in September than in March, while no significant seasonal variation was observed over Imperial.
234 Additionally, during the September campaign, afternoon NH$_3$ levels were 20–50 % higher than those measured in
235 the morning across both study areas.

236
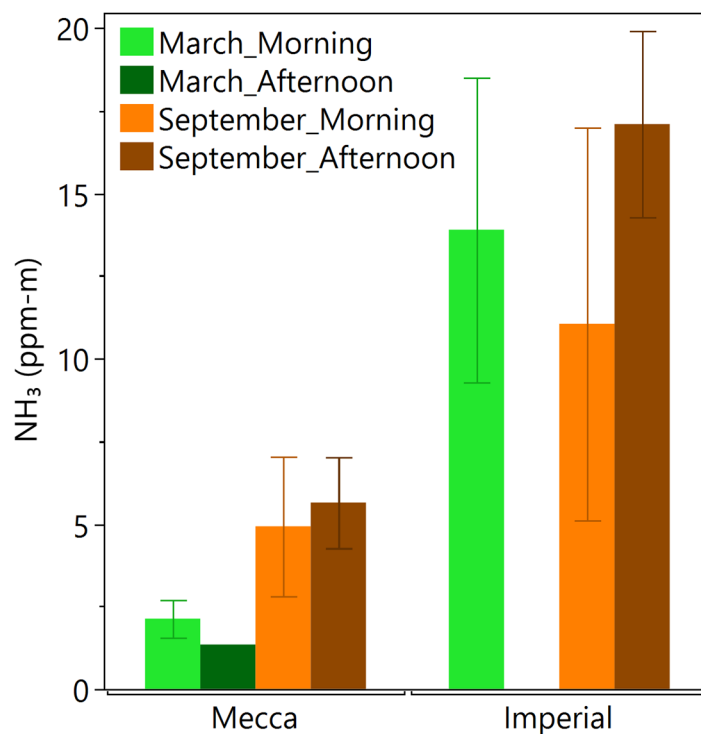
Figure 3. Average NH₃ column density (ppm-m) for each study area and airborne measurement session. Error bars represent one standard deviation across measurements from different flight lines in each study area.

Figures 4 and 5 illustrate NH₃ column density maps over Mecca and Imperial, respectively, from each airborne measurement session. Over Mecca in March, a distinct, strong plume was observed in the northwest part of the study area during the morning but dissipated by the afternoon. A closer examination of this plume in Figure S5 suggests it likely originated from a waste recycling facility located upwind, which was not fully captured during the March flight acquisition. As previously noted, in September, the flight measurements were extended northwestward to encompass this facility. The results showed detectable but relatively weaker plumes during both the morning and afternoon measurements. According to EPA TRI, this facility emitted over 27,500 pounds (12,470 kg) of NH₃ in 2023. Another notable observation over Mecca is the significant increase in NH₃ column density during the September afternoon measurements compared to the morning. The majority of hotspots were diffuse emissions concentrated over agricultural fields. This increase is likely due to higher afternoon temperatures, which enhance NH₃ volatilization from soil and plant surfaces, particularly in areas where fertilizers have been recently applied. Another possible explanation is the higher thermal contrast during the afternoon flights, which enhances the Mako sensor's detection sensitivity and enables the identification of NH₃ signals even at relatively low concentrations. Additional information about retrieval sensitivity can be found in the discussion section.
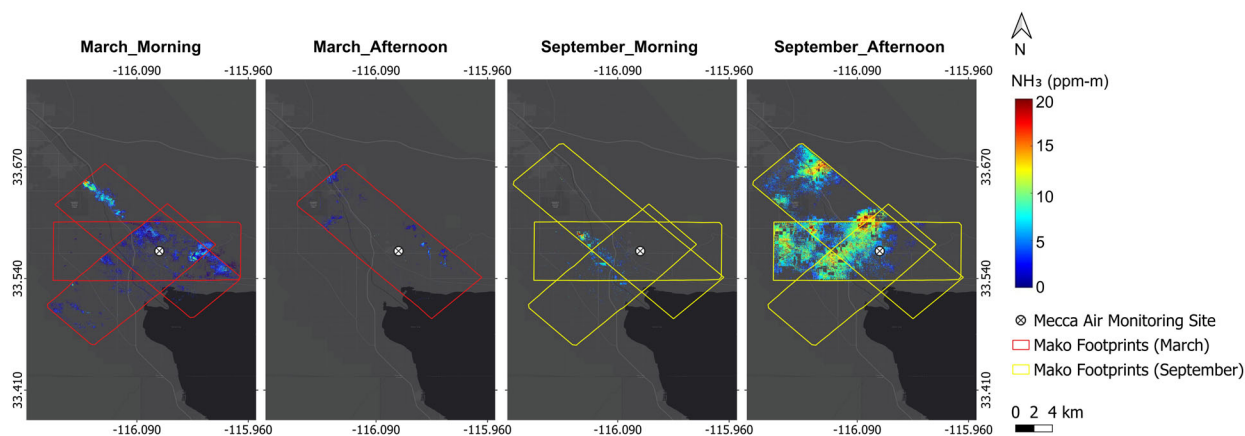
Figure 4. Retrieved NH₃ column density (ppm-m) maps over the Mecca study area during each airborne measurement session. Null pixels that did not meet the t-statistic and ΔT thresholds are rendered transparent. Map sources: Esri, HERE, Garmin, INCREMENT P, ©OpenStreetMap contributors, and the GIS User Community.
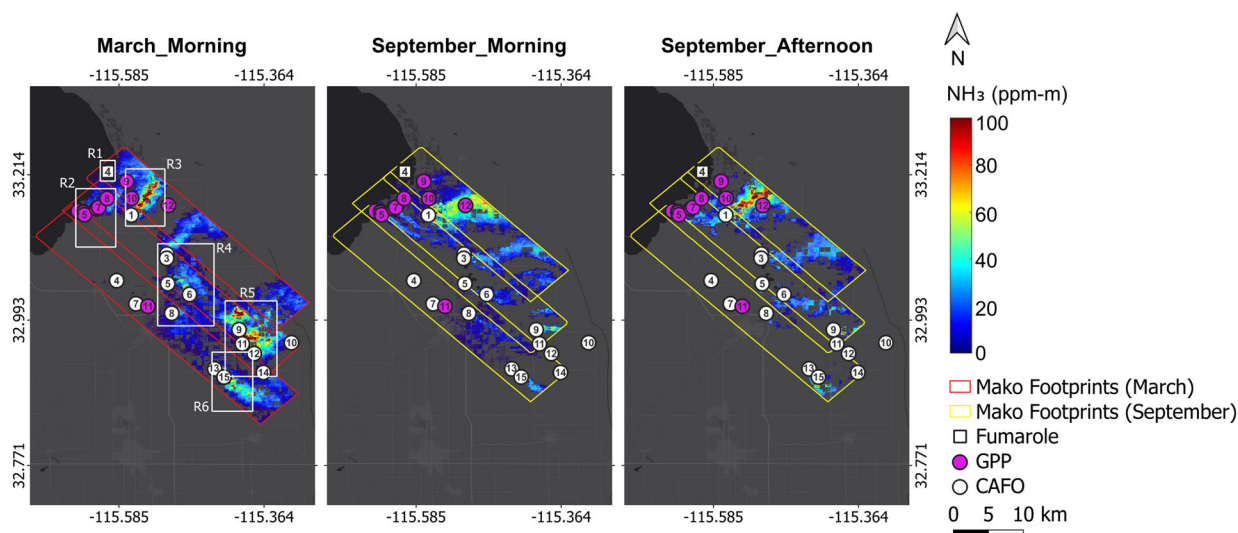
Figure 5. Retrieved NH₃ column density (ppm-m) maps over the Imperial study area during each airborne measurement session. Null pixels that did not meet the t-statistic and ΔT thresholds are rendered transparent. The markers in each panel denote known NH₃ emission sources. Six hotspot regions, shown with white boxes, are defined for further investigation. Map sources: Esri, HERE, Garmin, INCREMENT P, ©OpenStreetMap contributors, and the GIS User Community.

Significantly higher NH₃ levels were measured in the Imperial region. To properly illustrate the spatial gradient, the column density scale was adjusted from 0–20 ppm-m (used for the Mecca area) to 0–100 ppm-m. Multiple hotspots were detected in Imperial, and to identify the emitters, the locations of known point sources, including fumaroles, CAFO facilities, and GPPs, were overlaid on the maps (Figure 5). A version of these maps without the markers is included in the Supplementary Information Figure S6, to provide a clearer depiction of the detected plume patterns. Due to the complexity of this region, with several localized hotspots and sources in close proximity, six regions were

270   identified for further investigation (Figure 5). Moreover, Figure 6 depicts the pixel-level NH₃ column density

271   distributions in each region and flight measurement session.

272
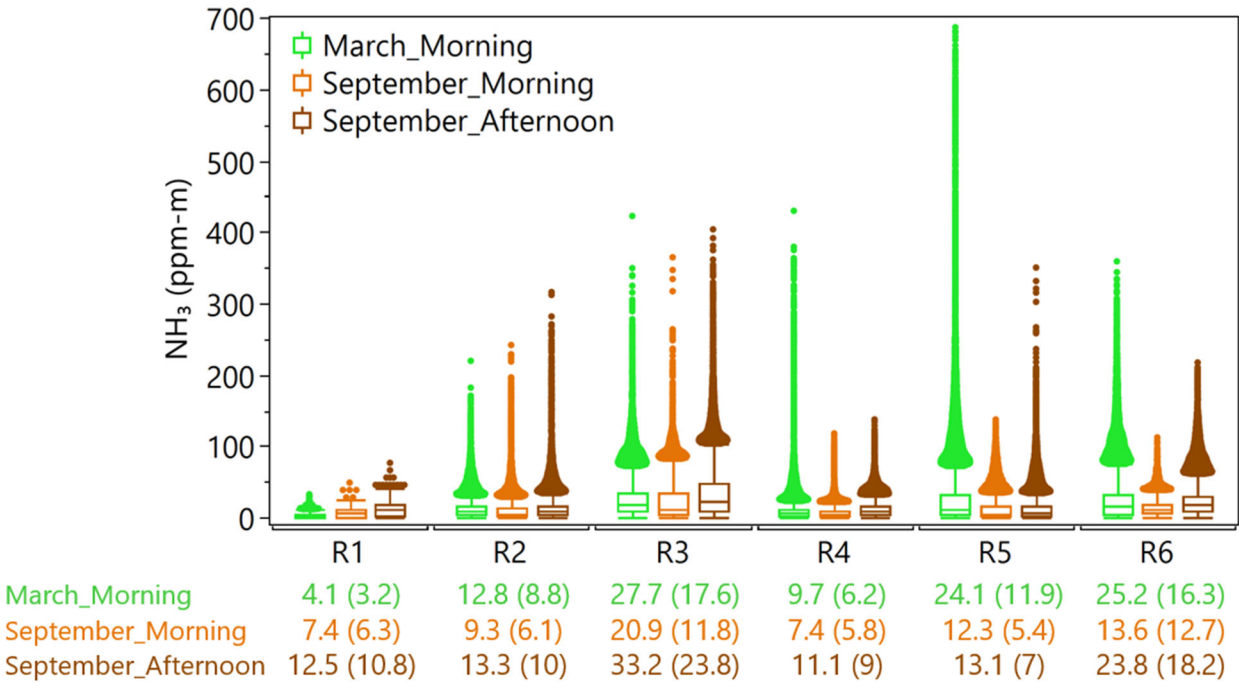
273   **Figure 6. Box plots of pixel-level retrieved NH₃ column density (ppm-m) for each predefined region and measurement**
274   **session over the Imperial study area. Boxes represent the interquartile range (IQR), with the horizontal line inside each**
275   **box indicating the median value. Whiskers extend to 1.5 times the IQR, and outliers are values exceeding 1.5 times the**
276   **IQR. Arithmetic mean (median) values are reported below the plot.**

277
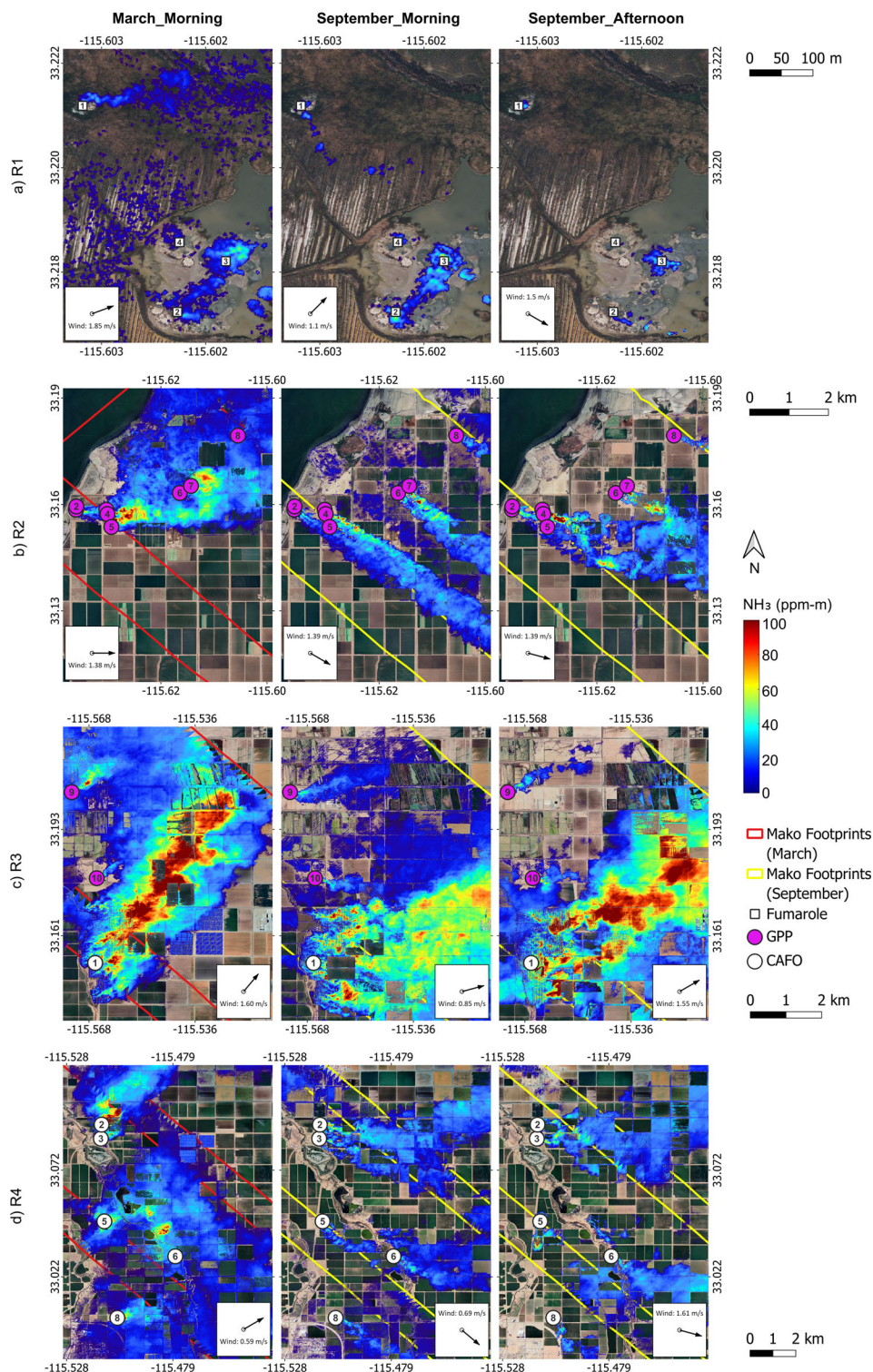
Figure 7 (a-d). Retrieved NH₃ column density (ppm-m) maps over predefined Regions 1–4 in the Imperial study area
during each airborne measurement session. Null pixels that did not meet the t-statistic and ΔT thresholds are rendered
transparent. The markers in each panel denote known NH₃ emission sources. Wind directions were inferred from plume
patterns, and average wind speeds were calculated from the nearest HRRR grid cells. **Base imagery** ~~Map data~~ **©2025**
Google.

283   Region 1 (Figure 7a) encompasses a number of known fumaroles along the southeastern shoreline of the Salton Sea,

284   that appear to be associated with the Calipatria Fault (Lynch and Hudnut, 2008). Measurements over this area

285   revealed fluctuating NH_3 emissions from these natural geothermal vents, though the levels were not as substantial as

286   other sources detected in the region. Across the three airborne acquisitions over this region, average NH_3 column

287   density ranged between 4.1 and 12.5 ppm-m. Fumaroles, associated with geothermal activity, emit NH_3 as

288   superheated water and gases interact with nitrogen-bearing, organic-rich sediments. This process triggers chemical

289   reactions and the thermal decomposition of organic matter, releasing NH_3 and other gases into the atmosphere (Tratt

290   et al., 2011). These emissions are inherently variable, influenced by factors such as the intensity of geothermal

291   activity, sediment composition, and local geological conditions (Tratt et al., 2016). The detection and quantification

292   of these emissions were made possible by the high-spatial resolution (~2 m) of LWIR imaging, which allowed for

293   the identification of emissions at a fine scale that would otherwise be undetectable.

294   Region 2 (Figure 7b) comprises eight known GPPs, with generating capacities ranging from 10 to 54 MW. Airborne

295   measurements detected NH_3 emissions from all of these facilities, consistently across both seasons and at different

296   times of the day. In the September morning measurements, the dispersion and overlap of NH_3 emissions from this

297   cluster of GPPs tracked to a distance of approximately 7.5 km downwind. Moreover, the use of high-spatial

298   resolution measurements allowed for precise localization of emission points within each facility. In nearly all plants,

299   NH_3 emissions were primarily concentrated around the cooling towers. Figure S7 shows zoomed-in views of

300   emissions over GPPs 6, 7, and 9, illustrating the highest NH_3 emissions from their cooling towers. This pattern is

301   consistent with standard operational procedures in geothermal plants, where NH_3 is separated from the geothermal

302   brine and vented through the cooling tower exhaust. This method of disposal is common in such facilities as it

303   enhances the overall efficiency of the power plant while preventing NH_3 from causing operational issues, such as

304   corrosion (Frick et al., 2019; Nogara and Zarrouk, 2018).

305   Region 3 (Figure 7c), which contains the largest CAFO and the highest-capacity GPP in the study area, consistently

306   recorded the highest average NH_3 column density among all regions during each flight session, ranging from 20.9 to

307   33.2 ppm-m, with maximum pixel-level values exceeding 350 ppm-m. The emissions from CAFO 1 were

308   remarkably large, with plumes that far outsized those of any other sources in the entire study area. Across the three

309   flight acquisitions over Region 3, the width of the plumes from CAFO 1 ranged from 2.2 to 2.8 km and extended 7.1

310   to 7.7 km downwind of the source. In comparison, plume widths and lengths from the two nearby GPPs in this

311   region ranged from 0.1 to 0.3 km and 1 to 2.7 km, respectively. CAFOs emit NH_3 primarily due to the breakdown of

312   nitrogen-rich compounds in livestock manure, particularly urea in urine. Urea undergoes enzymatic hydrolysis when

313   it comes into contact with fecal matter, producing NH_3 gas. Factors such as manure management, ambient

314   temperature, pH, and wind speed influence this process (Hiranuma et al., 2010; Hristov et al., 2011). As previously

315   noted, CAFO 1 has the largest cattle population in the state, which explains the substantial NH_3 emissions from this

316   facility.

317   Regions 4, 5, and 6 (Figures 7d and S8 a-b) each contain multiple CAFOs, with detectable emissions from every

318   facility during each flight measurement, though the magnitudes varied among facilities. Region 6, encompassing

CAFOs 13 and 15, exhibited the second-highest average NH_3 column densities during each flight measurement, with levels ranging from 13.6 to 25.2 ppm-m. CAFOs 2 and 9, which have the second and third largest cattle populations (Figure S3), displayed particularly high NH_3 emissions during the March morning measurements, with maximum pixel-level column densities reaching 400 and 700 ppm-m, respectively.

Closer examination of the NH_3 column density maps for Regions 4 and 5 revealed emissions from a few facilities not included in the known emission sources overlaid on the maps. Specifically, in Region 4, two detectable emission sources were identified north of CAFO 6. Similarly, in Region 5, a notable emission source was detected north of CAFO 9. Figure S9 provides a zoomed-in view of these sources, which appear to be CAFOs based on satellite imagery but were not listed in the CADD database. Notably, the emissions from the non-inventoried source north of CAFO 9 were particularly significant during the March morning measurements, with pixel-level NH_3 column densities far exceeding 100 ppm-m.

Overall, the airborne measurements demonstrated a strong capability in identifying NH_3 emission sources. Quantitatively, the surveys detected NH_3 emissions from all four known fumarole geothermal vents, all 12 GPPs, and all 13 known CAFOs within the study area. Additionally, the high spatial resolution enabled the identification of at least three previously uninventoried point emission sources, appearing as CAFOs based on satellite imagery but not listed in existing databases, highlighting the method's ability to discover undocumented emitters.

3.2. Ground-Based In-Situ Mobile Monitoring

Mobile NH_3 monitoring was conducted primarily between 8:00 AM and 6:00 PM, concurrent with airborne measurements over Mecca (March 28th) and Imperial (September 25th). Figures 8 and 1 illustrate the time series of ground-level NH_3 concentrations on each monitoring day and map of the areas covered by the mobile platform, respectively. Gaps in the time series plots (Figure 8) correspond to periods when the instrument operated outside its nominal temperature and flow rate ranges, resulting in unrecorded concentration measurements. NH_3 concentrations were significantly higher in Imperial compared to Mecca, with average levels of ~~250.1~~23.8 ppb in Mecca on March 28th and ~~5,769~~250.1 ppb in Imperial on September 25th. The time series plots reveal multiple distinct plumes in the Imperial study area, detected as the mobile platform passed various sources, while the Mecca measurements indicated only a single notable increase above the background levels. To pinpoint the locations and potential emission sources, individual plumes were first identified based on distinct peaks in the time series plot (Figure 8)~~in the time series plot (Figure 8) were labeled A to I~~, and their corresponding spatial locations were then mapped in Figure 9~~are presented in Figure 9~~. Additionally, Figure 10 compares NH_3 concentration distributions across the identified plumes and highlights nearby known sources as potential emission contributors. In interpreting the mobile monitoring data, it is important to consider that the recorded NH_3 levels reflect concentrations at the sampling height (~3m AGL) and, thus, any plumes passing above this height may not have been fully captured by the mobile platform.

352
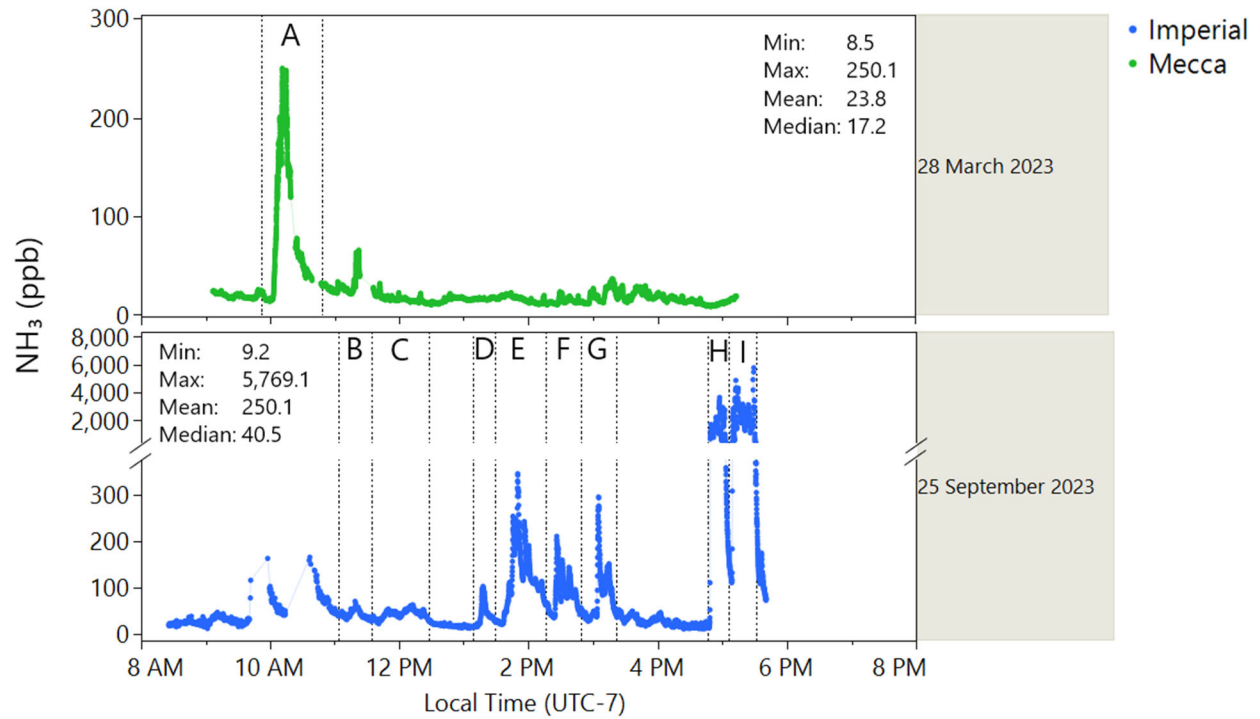
Figure 8. Time series of instantaneous ground-level NH₃ concentrations (ppb) measured by the mobile platform on each measurement day, with individual plumes labeled A to I for further investigation.

355
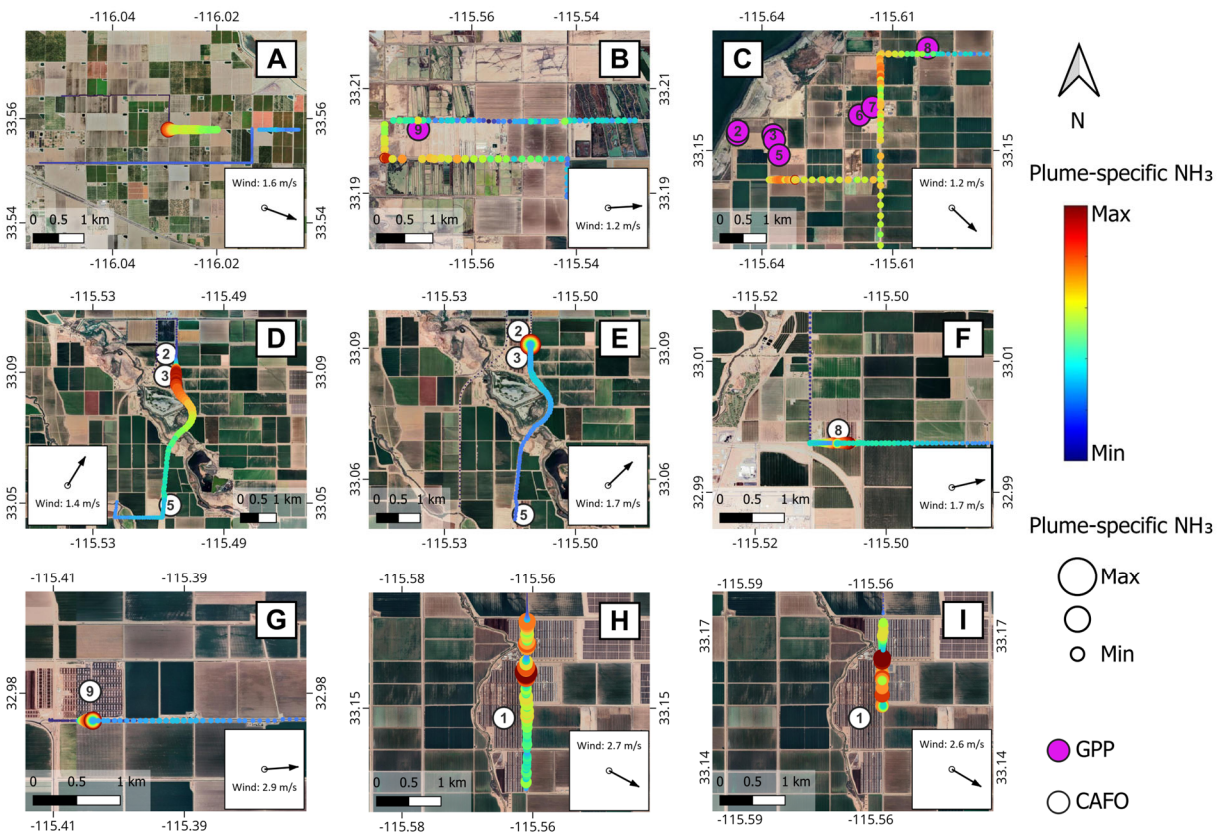
Figure 9. Maps of individual ground-level NH₃ plumes (A to I), as defined in Figure 8, measured by the mobile platform. The color bar and marker sizes represent the plume specific NH₃ range, where blue and red correspond to the minimum and maximum NH₃ values within each panel, respectively. Because scaling is performed separately for each plume, colors and marker sizes highlight spatial patterns within plumes but are not comparable across panels. Absolute concentrations and cross-plume comparisons are provided in Figures 8 and 10~~The color scale and marker sizes represent relative NH₃ values, with absolute values provided in Figures 8 and 10. Locations of potential known sources near each identified plume are indicated using various markers on the map~~. Average wind speed and direction were calculated from the nearest HRRR grid cells. Base imagery ~~Map data~~ **©2025 Google.**

As shown in Figure 9, nearly all identified plumes, except for plume A, were detected near known NH₃ emission sources. Plume A, the only notable plume detected by the mobile platform in the Mecca study area in March, was observed around some agricultural fields, suggesting NH₃ emissions from fertilizer volatilization. Concurrent airborne NH₃ imagery confirmed that Plume A originated from a diffuse area source linked to the surrounding agricultural fields. Ground observations by the field team also verified that the fields had been freshly fertilized. Ground-level NH₃ concentrations measured near CAFOs were generally higher compared to those recorded downwind of GPPs (Figure 10). The highest NH₃ concentrations were consistently observed near CAFO 1, where the mobile platform recorded substantially elevated NH₃ levels—up to 5,700 ppb—each time it passed downwind of this source.
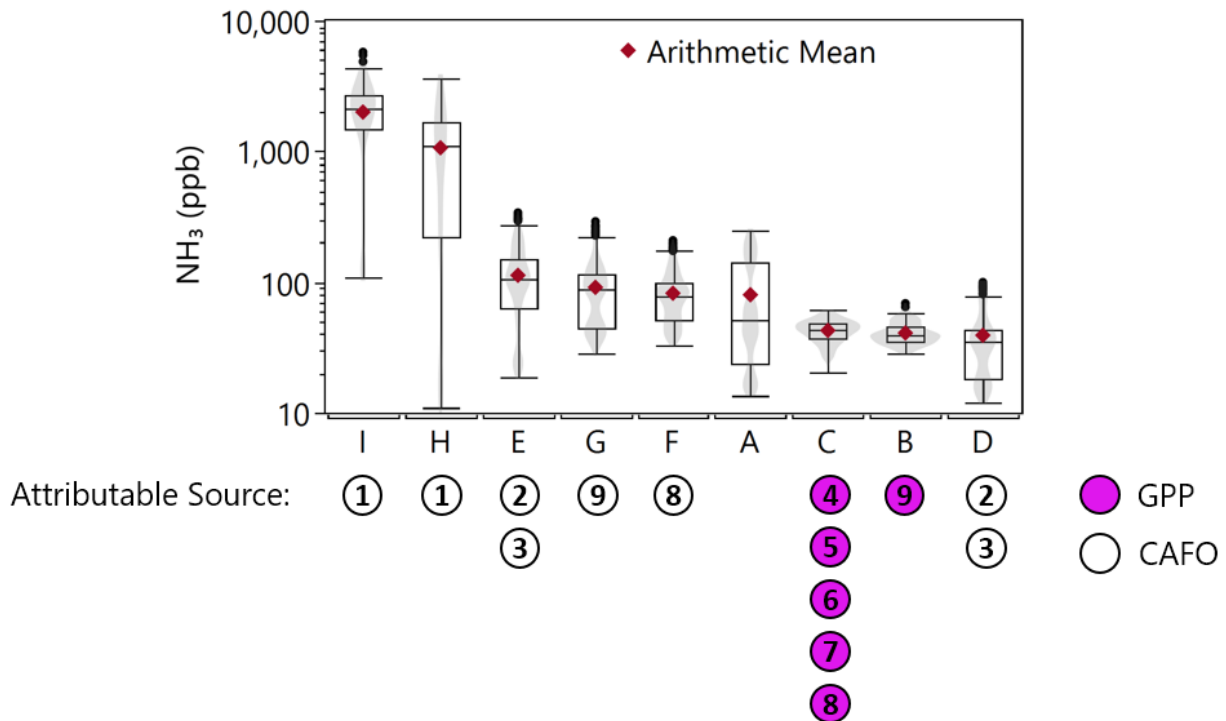
Figure 10. Box plots of ground-level NH₃ concentrations (ppb) for individual plumes (A to I), as defined in Figure 8, measured by the mobile platform, along with the potential attributable sources. Boxes represent the interquartile range (IQR), with the horizontal line inside each box indicating the median value. Whiskers extend to 1.5 times the IQR, and outliers are values exceeding 1.5 times the IQR. Arithmetic mean values are shown as red diamonds.

378   **3.3. Ground-Based In-Situ Stationary Monitoring**

379   As previously noted, the NH_3 monitor at the Mecca AMS was non-operational in March. Consequently, only the

380   NH_3 data from September 25th was used to validate airborne NH_3 measurements on that day, as described in detail

381   by Tratt et al. (2025). This section presents the longer-term temporal trends and directional patterns of NH_3 at this

382   site, providing insights into its characteristics in the Mecca region. Figure 11 illustrates the monthly averaged NH_3

383   concentrations, showing two notable maxima in winter and late summer, with minima in spring and late fall. Using

384   April concentrations as a proxy for March, NH_3 levels in September, when the second airborne campaign was

385   conducted, were found to be more than twice those recorded in April. Additionally, a comparison of average NH_3

386   levels across weekdays and weekends (Figure ~~S11~~S10) shows no significant differences, suggesting minimal

387   contributions from sources such as traffic to NH_3 emissions in this region.

388
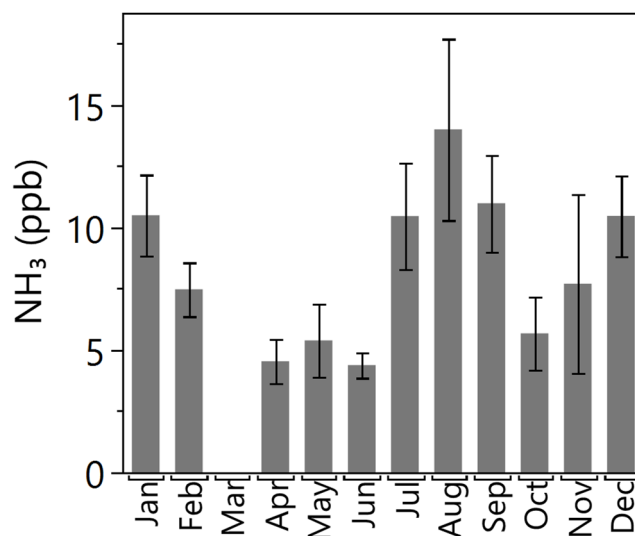
389   **Figure 11. Monthly averaged ground-level NH_3 concentrations (ppb) measured at the Mecca air monitoring site in 2023.**
390   **Error bars represent confidence intervals. March data is missing due to the NH_3 monitor being non-operational during**
391   **that period.**

392   The monthly bivariate polar plots in Figure ~~S12~~S11 indicate that wind patterns at Mecca are generally balanced

393   between the northwest and southeast directions. Notably, elevated NH_3 levels are most strongly associated with

394   southeasterly winds, with peak concentrations observed in January, July, August, September, and December. This

395   pattern points to the likely presence of an NH_3 source—or multiple sources—southeast of the Mecca AMS. Given

396   that the Imperial region, located southeast of Mecca, is known for significantly high NH_3 emissions, these emissions

397   are likely the main contributors to the elevated NH_3 concentrations measured at the Mecca AMS.

398   **4. Discussion**

399   Pronounced variations in NH_3 levels were observed over space and time within the study areas, and the tri-platform

400   approach provided complementary perspectives in capturing these spatiotemporal trends. Average NH_3 levels

401   measured by the airborne platform were found to be over eight times higher in Imperial compared to Mecca during

the March campaign, and approximately 2.5 times higher during the September campaign. Similarly, mobile
monitoring revealed nearly ten times higher average NH$_3$ levels in Imperial compared to Mecca. Directional analysis
at the Mecca AMS indicated that emissions from Imperial likely contribute to elevated NH$_3$ levels in Mecca.
Seasonally, the average NH$_3$ column densities over Mecca were approximately 3.5 times higher in September than in
March, while average levels in Imperial remained comparable across both seasons. The seasonal trend observed by
the airborne imaging instrument in Mecca aligns closely with stationary measurements from the Mecca AMS, which
recorded NH$_3$ levels over 2.5 times higher in September compared to April (used as a proxy for March, as the NH$_3$
monitor was non-operational).

The emission dynamics between the two study areas were notably distinct. Mecca exhibited considerably lower NH$_3$
emissions, with the most prominent point source identified being a waste recycling facility. In contrast, Imperial
presented a densely packed array of discrete sources, including several fumaroles, GPPs, and CAFOs. Among them,
CAFO facilities proved to be significant contributors, with larger cattle populations correlating with higher NH$_3$
emissions, consistent with findings of Kuai et al. (2019). Due to the dispersed layout of CAFO facilities, their
plumes were found to be more expansive compared to those of GPPs, which were narrower and more isolated,
predominantly concentrated around cooling towers. However, more accurate and quantitative assessment of
emissions from different sources requires emission flux calculations, which, as mentioned above, is the focus of
another publication from this field campaign.

The measurements presented here reinforce and expand understanding from previous research on atmospheric
ammonia using airborne, satellite, and modeling approaches. For example, Kuai et al. (2019) utilized airborne
HyTES measurements with 2 m spatial resolution in the California San Joaquin Valley to detect NH$_3$ enhancements
from cattle feedlots, power plants, and smoldering fires, reporting concentrations up to five times higher over
feedlots compared to power plants—findings that closely align with the plume magnitudes and spatial variability
observed in this study. Wang et al. (2021) oversampled IASI satellite data over the contiguous U.S. (CONUS) from
2008 to 2017 to produce ~2-km resolution monthly NH$_3$ maps, consistently identifying the Imperial Valley as a
hotspot with higher levels in September compared to March, consistent with our findings. Similarly, Pleim et al.
(2019) employed the CMAQ model coupled with the EPIC agricultural model over CONUS to simulate
bidirectional ammonia fluxes, highlighting the significant influence of agricultural fertilizer and livestock emissions
in California's Central and Imperial Valleys.

NH$_3$ emissions from CAFOs are an emerging concern, particularly with the growing number of these facilities
across the U.S. and the limited understanding of their emissions (Burns et al., 2023; Epps et al., 2025). This gap is
primarily due to the lack of reliable data on the number, size, and precise locations of CAFOs. Consequently, a
significant portion of CAFOs is missing from emission inventories. In fact, a review of the EPA's 2021 National
Emissions Inventory (https://www.epa.gov/air-emissions-inventories/national-emissions-inventory-nei, accessed
January 4, 2025) revealed no records of any CAFOs in our study areas, including CAFO 1, which, according to
CARB's CADD, is the largest CAFO in California, and our measurements revealed substantial emissions from this
facility.

438 High-spatial resolution, wide-area airborne LWIR imaging provided unprecedented insights into the identification

439 and quantification of NH$_3$ sources. The wide-area coverage enabled the survey of relatively large regions within a

440 short time, capturing all known sources and identifying previously unknown/unreported ones. Simultaneously, the

441 high-spatial resolution mapping at 2.1 m facilitated the detection of hotspots and the tracing of emission plumes

442 back to their release points, including isolated and relatively weak NH$_3$ sources such as fumaroles. In contrast,

443 existing satellite instruments capable of measuring atmospheric NH$_3$ (e.g., CrIS, IASI, AIRS) offer spatial

444 resolutions of 15–50 km, which are too coarse to resolve localized features. To illustrate this, a hypothetical 15 km x

445 15 km grid, representative of the finest satellite resolution currently available, was overlaid on an NH$_3$ column

446 density map from this study (Figure S12). As shown, nearly the entire cluster of geothermal power plants, all

447 fumaroles, and CAFO 1, the largest in the study area, can fall within a single satellite pixel, masking the spatial

448 variability captured by the airborne measurements. Additionally, ~~this approach~~airborne measurement allowed for

449 monitoring areas that are difficult to access with traditional ground-based or in-situ airborne methods. Another

450 important advantage of airborne remote sensing, which provides column data, is its ability to capture entire plumes.

451 Surface or airborne in-situ measurements, by contrast, may miss these plumes due to underflying, overflying, or

452 underdriving the plumes. Therefore, airborne remote sensing is an ideal tool for air quality managers and regulators

453 for surveying a wide target area to identify hotspots and guide their subsequent longer-term in-situ monitoring.

454 While LWIR hyperspectral imaging is highly effective in detecting, identifying, and tracking NH$_3$ emissions, its

455 sensitivity relies heavily on thermal contrast (Buckland et al., 2017; Hulley et al., 2016; Kuai et al., 2019). When

456 this contrast is small, as is often the case during early-morning hours before the ground has warmed, the sensor's

457 ability to detect low-level NH$_3$ diminishes. This effect was particularly evident in Mecca, where background NH$_3$

458 levels were already significantly lower than those in Imperial. Conversely, afternoon flights benefited from

459 increased solar heating, which raised ΔT and improved detection sensitivity, allowing the instrument to capture NH$_3$

460 signals more effectively, even at relatively low ambient concentrations. For example, on September 25th, the

461 stationary ground monitor at the Mecca AMS recorded similar NH$_3$ ambient concentrations during both morning and

462 afternoon flight times (around 4 ppb). However, as shown in Figure 4, the airborne measurements detected much

463 more widespread NH$_3$ signals in the afternoon. This difference was due to the higher average ΔT in the afternoon

464 (8.5 °C) compared to the morning (4 °C), which enabled the LWIR instrument to resolve NH$_3$ signatures more

465 effectively. More in-depth discussion about the sensitivity of the Mako retrievals in this study is provided in Tratt et

466 al. (2025).

467 Airborne remote sensing measurements inherently provide only "snapshots" of advected emissions within the

468 specific times and locations where data are collected. However, repeated measurements can offer insights into

469 typical conditions. Both JPL's HyTES and The Aerospace Corporation's Mako instruments have flown extensively

470 across California and selected regions worldwide, consistently detecting ubiquitous NH$_3$ emissions in urban and

471 rural areas (Buckland et al., 2017; Hulley et al., 2016; Kuai et al., 2019). Yet, no systematic effort has been made to

472 quantify these emissions. Extensive, long-term historical datasets from these instruments, combined with available

473   NH$_3$ retrieval algorithms with a good understanding of their uncertainties, present a unique opportunity to identify

474   and characterize NH$_3$ sources on a much broader scale.

475   A more cost-effective alternative for achieving broader area coverage and routine observations is satellite-borne

476   remote sensing. However, existing satellite LWIR instruments capable of measuring NH$_3$ lack the spatial resolution

477   needed to discern emissions at the local scale, especially in areas with dense sources, such as the Imperial region

478   studied here. Advances in hyperspectral infrared imaging spectrometers and high-resolution detector technologies

479   now enable NH$_3$ mapping from space-based instruments with higher spatial resolution. For instance, the European

480   Space Agency recently proposed Nitrosat, a satellite mission concept for high-resolution NH$_3$ monitoring, with

481   swaths over 80 km and a spatial resolution of 500 m (Noppen et al., 2023). Although not yet selected for further

482   development, Nitrosat represents significant progress in this area. Additionally, emerging High Operating

483   Temperature (HOT) Barrier Infrared Detectors (HOT BIRDs) technology (Wright et al., 2020) offers the potential

484   for lightweight, multi-band infrared detectors with minimal cooling requirements. These detectors can provide

485   space-based LWIR imaging at the spatial resolutions needed to monitor localized NH$_3$ sources, making them

486   promising for future advancements in NH$_3$ monitoring.

5.   Conclusions

488   NH$_3$ is increasingly recognized as an emerging pollutant of concern due to its role in secondary PM$_{2.5}$ formation and

489   nitrogen deposition, both of which have significant environmental and public health impacts. Accurate

490   characterization of NH$_3$ emissions is essential for improving emission inventories and developing more effective air

491   quality management strategies. This study demonstrates the integration of airborne LWIR hyperspectral imaging

492   with ground-based stationary and mobile monitoring for mapping and characterizing NH$_3$ emissions at hyperlocal

493   scales across two distinct seasons in the Salton Sea region. Seasonal differences were notable over Mecca, with NH$_3$

494   column densities approximately 3.5 times higher in September than in March, while levels in Imperial remained

495   relatively comparable across seasons. The high spatial resolution of the LWIR imager revealed pronounced spatial

496   variability in NH$_3$ levels, with Imperial exhibiting average NH$_3$ column densities 2.5 to 8 times ~~significantly~~ higher

497   ~~levels~~ than Mecca—a disparity primarily driven by sources such as CAFOs, geothermal power plants, fumaroles,

498   and intensive agricultural activities. Notably, the ability to detect previously unreported emission sources, especially

499   in densely populated agricultural areas, underscores the potential of this approach to improve the identification and

500   characterization of NH$_3$ emission sources. These findings provide key insights into local-scale emission patterns that

501   are often missed by traditional ground-based or satellite measurements, highlighting the need for more routine,

502   wide-scale airborne campaigns and the development of new satellite missions with enhanced resolution to fill

503   critical data gaps.

504   **Data availability**

505   Data from this study can be made available upon request.

506   **Author Contributions**

Conceptualization: SH, DMT, and OVK; methodology: DMT, CSC, SH, and OVK; flight planning and airborne data acquisition: ERK; airborne data processing: CSC and KNB; data visualization and plume dispersion analysis: CSC; ground mobile data acquisition and processing: YM; meteorological model data: MA; stationary measurements: PP and MS; writing—original draft: SH; writing—review and editing: all authors. All authors have read and approved the final version of the manuscript.

Competing interests

The authors declare that they have no conflict of interest.

Acknowledgments

This research was conducted at the Jet Propulsion Laboratory, California Institute of Technology, under a contract with NASA, with support from The Aerospace Corporation's Independent Research and Development program, and Research and Technology Collaborations Office, and the University of California, Riverside. We would like to thank Drs. Toshihiro Kuwayama and Morteza Amini for their valuable input and thoughtful perspectives, which significantly enriched this work. The views and conclusions expressed in this paper are those of the authors and do not necessarily reflect the official policies or positions of their affiliated institutions.

References

Adams, P. M., Lynch, D. K., Buckland, K. N., Johnson, P. D., and Tratt, D. M.: Sulfate mineralogy of fumaroles in the Salton Sea Geothermal Field, Imperial County, California, Journal of Volcanology and Geothermal Research, 347, 15–43, https://doi.org/10.1016/j.jvolgeores.2017.08.010, 2017.

Beaudor, M., Hauglustaine, D., Lathière, J., Van Damme, M., Clarisse, L., and Vuichard, N.: Evaluating present-day and future impacts of agricultural ammonia emissions on atmospheric chemistry and climate, Atmospheric Chemistry and Physics, 25, 2017–2046, https://doi.org/10.5194/acp-25-2017-2025, 2025.

Bi, J., Stowell, J., Seto, E. Y. W., English, P. B., Al-Hamdan, M. Z., Kinney, P. L., Freedman, F. R., and Liu, Y.: Contribution of low-cost sensor measurements to the prediction of PM2.5 levels: A case study in Imperial County, California, USA, Environmental Research, 180, 108810, https://doi.org/10.1016/j.envres.2019.108810, 2020.

Buckland, K. N., Young, S. J., Keim, E. R., Johnson, B. R., Johnson, P. D., and Tratt, D. M.: Tracking and quantification of gaseous chemical plumes from anthropogenic emission sources within the Los Angeles Basin, Remote Sensing of Environment, 201, 275–296, https://doi.org/10.1016/j.rse.2017.09.012, 2017.

Burns, A. M., Chandler, G., Dunham, K. J., and Carlton, A. G.: Data Gap: Air Quality Networks Miss Air Pollution from Concentrated Animal Feeding Operations, Environ. Sci. Technol., 57, 20718–20725, https://doi.org/10.1021/acs.est.3c06947, 2023.

Dammers, E., McLinden, C. A., Griffin, D., Shephard, M. W., Van Der Graaf, S., Lutsch, E., Schaap, M., Gainairu-Matz, Y., Fioletov, V., Van Damme, M., Whitburn, S., Clarisse, L., Cady-Pereira, K., Clerbaux, C., Coheur, P. F., and Erisman, J. W.: NH3 emissions from large point sources derived from CrIS and IASI satellite observations, Atmospheric Chemistry and Physics, 19, 12261–12293, https://doi.org/10.5194/acp-19-12261-2019, 2019.

Epps, A., Dressel, I. M., Guo, X., Odanibe, M., Fields, K. P., Carlton, A. M. G., Sun, K., and Pusede, S. E.: Satellite Observations of Atmospheric Ammonia Inequalities Associated with Industrialized Swine Facilities in Eastern North Carolina, Environ. Sci. Technol., 59, 2651–2664, https://doi.org/10.1021/acs.est.4c11922, 2025.

544   European Commission: Proposal for a Directive of the European Parliament and of the Council on the Energy
545   Performance of Buildings (recast), 2022.

546   Farzan, S. F., Razafy, M., Eckel, S. P., Olmedo, L., Bejarano, E., and Johnston, J. E.: Assessment of Respiratory
547   Health Symptoms and Asthma in Children near a Drying Saline Lake, International Journal of Environmental
548   Research and Public Health, 16, 3828, https://doi.org/10.3390/ijerph16203828, 2019.

549   Felix, J. D., Elliott, E. M., and Gay, D. A.: Spatial and temporal patterns of nitrogen isotopic composition of
550   ammonia at U.S. ammonia monitoring network sites, Atmospheric Environment, 150, 434–442,
551   https://doi.org/10.1016/j.atmosenv.2016.11.039, 2017.

552   Frick, S., Kranz, S., Kupfermann, G., Saadat, A., and Huenges, E.: Making use of geothermal brine in Indonesia:
553   binary demonstration power plant Lahendong/Pangolombian, Geothermal Energy, 7, 30,
554   https://doi.org/10.1186/s40517-019-0147-2, 2019.

555   Frie, A. L., Garrison, A. C., Schaefer, M. V., Bates, S. M., Botthoff, J., Maltz, M., Ying, S. C., Lyons, T., Allen, M.
556   F., Aronson, E., and Bahreini, R.: Dust Sources in the Salton Sea Basin: A Clear Case of an Anthropogenically
557   Impacted Dust Budget, Environ. Sci. Technol., 53, 9378–9388, https://doi.org/10.1021/acs.est.9b02137, 2019.

558   Hall, J. L., Boucher, R. H., Gutierrez, D. J., Hansel, S. J., Kasper, B. P., Keim, E. R., Moreno, N. M., Polak, M. L.,
559   Sivjee, M. G., Tratt, D. M., and Warren, D. W.: First flights of a new airborne thermal infrared imaging spectrometer
560   with high area coverage, in: Infrared Technology and Applications XXXVII, Infrared Technology and Applications
561   XXXVII, 47–53, https://doi.org/10.1117/12.884865, 2011.

562   Hall, J. L., Boucher, R. H., Buckland, K. N., Gutierrez, D. J., Keim, E. R., Tratt, D. M., and Warren, D. W.: Mako
563   airborne thermal infrared imaging spectrometer: performance update, in: Imaging Spectrometry XXI, Imaging
564   Spectrometry XXI, 997604, https://doi.org/10.1117/12.2239245, 2016.

565   Hall, J. L., Chang, C. S., Westberg, K., and Tratt, D. M.: Scene Analysis for Gas Estimation (SAGE): A tool for
566   quantification of diffuse and point-source atmospheric trace gas abundance, Remote Sensing of Environment, 2025.

567   Hiranuma, N., Brooks, S. D., Thornton, D. C. O., and Auvermann, B. W.: Atmospheric Ammonia Mixing Ratios at
568   an Open-Air Cattle Feeding Facility, Journal of the Air & Waste Management Association, 60, 210–218,
569   https://doi.org/10.3155/1047-3289.60.2.210, 2010.

570   Hristov, A. N., Hanigan, M., Cole, A., Todd, R., McAllister, T. A., Ndegwa, P. M., and Rotz, A.: Review: Ammonia
571   emissions from dairy farms and beef feedlots, Can. J. Anim. Sci., 91, 1–35, https://doi.org/10.4141/CJAS10034,
572   2011.

573   Hulley, G. C., Duren, R. M., Hopkins, F. M., Hook, S. J., Vance, N., Guillevic, P., Johnson, W. R., Eng, B. T.,
574   Mihaly, J. M., Jovanovic, V. M., Chazanoff, S. L., Staniszewski, Z. K., Kuai, L., Worden, J., Frankenberg, C.,
575   Rivera, G., Aubrey, A. D., Miller, C. E., Malakar, N. K., Sánchez Tomás, J. M., and Holmes, K. T.: High spatial
576   resolution imaging of methane and other trace gases with the airborne Hyperspectral Thermal Emission
577   Spectrometer (HyTES), Atmospheric Measurement Techniques, 9, 2393–2408, https://doi.org/10.5194/amt-9-2393-
578   2016, 2016.

579   Johnston, J. E., Razafy, M., Lugo, H., Olmedo, L., and Farzan, S. F.: The disappearing Salton Sea: A critical
580   reflection on the emerging environmental threat of disappearing saline lakes and potential impacts on children's
581   health, Science of The Total Environment, 663, 804–817, https://doi.org/10.1016/j.scitotenv.2019.01.365, 2019.

582   Johnston, J. E., Kamai, E., Duenas Barahona, D., Olmedo, L., Bejarano, E., Torres, C., Zuidema, C., Seto, E., Eckel,
583   S. P., and Farzan, S. F.: Air quality and wheeze symptoms in a rural children's cohort near a drying saline lake,
584   Environmental Research, 263, 120070, https://doi.org/10.1016/j.envres.2024.120070, 2024.

Jones, B. A. and Fleck, J.: Shrinking lakes, air pollution, and human health: Evidence from California's Salton Sea, Science of The Total Environment, 712, 136490, https://doi.org/10.1016/j.scitotenv.2019.136490, 2020.

Kuai, L., Kalashnikova, O. V., Hopkins, F. M., Hulley, G. C., Lee, H., Garay, M. J., Duren, R. M., Worden, J. R., and Hook, S. J.: Quantification of Ammonia Emissions With High Spatial Resolution Thermal Infrared Observations From the Hyperspectral Thermal Emission Spectrometer (HyTES) Airborne Instrument, IEEE Journal of Selected Topics in Applied Earth Observations and Remote Sensing, 12, 4798–4812, https://doi.org/10.1109/JSTARS.2019.2918093, 2019.

Kuttippurath, J., Patel, V. K., Kashyap, R., Singh, A., and Clerbaux, C.: Anomalous increase in global atmospheric ammonia during COVID-19 lockdown: Need policies to curb agricultural emissions, Journal of Cleaner Production, 434, 140424, https://doi.org/10.1016/j.jclepro.2023.140424, 2024.

Leifer, I., Melton, C., Tratt, D. M., Buckland, K. N., Clarisse, L., Coheur, P., Frash, J., Gupta, M., Johnson, P. D., Leen, J. B., Van Damme, M., Whitburn, S., and Yurganov, L.: Remote sensing and *in situ* measurements of methane and ammonia emissions from a megacity dairy complex: Chino, CA, Environmental Pollution, 221, 37–51, https://doi.org/10.1016/j.envpol.2016.09.083, 2017.

Li, W., Wang, X., Song, W., Zhang, Z., Wang, X., Liu, X., Ma, T., Wang, Q., Zhang, Y., Wang, X., and Geng, L.: On the contribution of atmospheric reactive nitrogen deposition to nitrogen burden in a eutrophic Lake in eastern China, Water Research, 268, 122597, https://doi.org/10.1016/j.watres.2024.122597, 2025.

Lieb, H. C., Maldonado, M., Ruiz, E., Torres, C., Olmedo, L., Walters, W. W., and Faloona, I. C.: Nitrogen isotopes reveal high NOx emissions from arid agricultural soils in the Salton Sea Air Basin, Sci Rep, 14, 28725, https://doi.org/10.1038/s41598-024-78361-y, 2024.

Lynch, D. K. and Hudnut, K. W.: The Wister Mud Pot Lineament: Southeastward Extension or Abandoned Strand of the San Andreas Fault?, Bulletin of the Seismological Society of America, 98, 1720–1729, https://doi.org/10.1785/0120070252, 2008.

Ma, J., Shi, H., Zhu, Y., Li, R., Wang, S., Lu, N., Yao, Y., Bian, Z., and Huang, K.: The Evolution of Global Surface Ammonia Concentrations during 2001–2019: Magnitudes, Patterns, and Drivers, Environ. Sci. Technol., 59, 5066–5079, https://doi.org/10.1021/acs.est.4c14020, 2025.

Miao, Y., Porter, W. C., Benmarhnia, T., Lowe, C., Lyons, T. W., Hung, C., and Diamond, C.: Source-specific acute cardio-respiratory effects of ambient coarse particulate matter exposure in California's Salton Sea region, Environ. Res.: Health, 3, 015006, https://doi.org/10.1088/2752-5309/ad934a, 2025.

Nair, A. A. and Yu, F.: Quantification of Atmospheric Ammonia Concentrations: A Review of Its Measurement and Modeling, Atmosphere, 11, 1092, https://doi.org/10.3390/atmos11101092, 2020.

Nogara, J. and Zarrouk, S. J.: Corrosion in geothermal environment: Part 1: Fluids and their impact, Renewable and Sustainable Energy Reviews, 82, 1333–1346, https://doi.org/10.1016/j.rser.2017.06.098, 2018.

Noppen, L., Clarisse, L., Tack, F., Ruhtz, T., Merlaud, A., Van Damme, M., Van Roozendael, M., Schuettemeyer, D., and Coheur, P.: Constraining industrial ammonia emissions using hyperspectral infrared imaging, Remote Sensing of Environment, 291, 113559, https://doi.org/10.1016/j.rse.2023.113559, 2023.

Pleim, J. E., Ran, L., Appel, W., Shephard, M. W., and Cady-Pereira, K.: New Bidirectional Ammonia Flux Model in an Air Quality Model Coupled With an Agricultural Model, Journal of Advances in Modeling Earth Systems, 11, 2934–2957, https://doi.org/10.1029/2019MS001728, 2019.

Shephard, M. W., Dammers, E., Cady-Pereira, K. E., Kharol, S. K., Thompson, J., Gainariu-Matz, Y., Zhang, J., McLinden, C. A., Kovachik, A., Moran, M., Bittman, S., Sioris, C. E., Griffin, D., Alvarado, M. J., Lonsdale, C., Savic-Jovcic, V., and Zheng, Q.: Ammonia measurements from space with the Cross-track Infrared Sounder:

627 characteristics and applications, Atmospheric Chemistry and Physics, 20, 2277–2302, https://doi.org/10.5194/acp-
628 20-2277-2020, 2020.

629 South Coast AQMD: South Coast Air Basin Attainment Plan for the 2012 Annual PM2.5 Standard, 2024.

630 Tang, K., Zhang, H., Xu, G., Chang, F., Xu, Y., Miao, J., Cui, X., Jin, J., Li, B., Li, K., Liao, H., and Li, N.:
631 Optimizing Ammonia Emissions for $PM_{2.5}$ Mitigation: Environmental and Health Co-Benefits in Eastern China,
632 EGUsphere, 1–35, https://doi.org/10.5194/egusphere-2025-1407, 2025.

633 Tratt, D. M., Young, S. J., Lynch, D. K., Buckland, K. N., Johnson, P. D., Hall, J. L., Westberg, K. R., Polak, M. L.,
634 Kasper, B. P., and Qian, J.: Remotely sensed ammonia emission from fumarolic vents associated with a
635 hydrothermally active fault in the Salton Sea Geothermal Field, California, Journal of Geophysical Research:
636 Atmospheres, D21308, 116, https://doi.org/10.1029/2011JD016282, 2011.

637 Tratt, D. M., Buckland, K. N., Young, S. J., Johnson, P. D., Riesz, K. A., and Molina, K. C.: Remote sensing
638 visualization and quantification of ammonia emission from an inland seabird colony, JARS, 7, 073475,
639 https://doi.org/10.1117/1.JRS.7.073475, 2013.

640 Tratt, D. M., Young, S. J., Johnson, P. D., Buckland, K. N., and Lynch, D. K.: Multi-year study of remotely-sensed
641 ammonia emission from fumaroles in the Salton Sea Geothermal Field, in: 2016 8th Workshop on Hyperspectral
642 Image and Signal Processing: Evolution in Remote Sensing (WHISPERS), 2016 8th Workshop on Hyperspectral
643 Image and Signal Processing: Evolution in Remote Sensing (WHISPERS), 1–5,
644 https://doi.org/10.1109/WHISPERS.2016.8071692, 2016.

645 Tratt, D. M., Chang, C. S., Keim, E. R., Buckland, K. N., Alvarez, M., Kalashnikova, O., Hasheminassab, S., Garay,
646 M. J., Miao, Y., Porter, W. C., Hopkins, F. M., Pakbin, P., and Sowlat, M.: Airborne Mapping of Atmospheric
647 Ammonia in a Mixed Discrete and Diffuse Emission Environment, Remote Sensing, 17, 95,
648 https://doi.org/10.3390/rs17010095, 2025.

649 Current Nonattainment Counties for All Criteria Pollutants:
650 https://www3.epa.gov/airquality/greenbook/ancl.html?utm_source=chatgpt.com, last access: 4 January 2025.

651 Reconsideration of the National Ambient Air Quality Standards for Particulate Matter, 88 Fed. Reg. 5558 | Casetext:
652 https://casetext.com/federal-register/reconsideration-of-the-national-ambient-air-quality-standards-for-particulate-
653 matter, last access: 4 January 2025.

654 Van Damme, M., Clarisse, L., Franco, B., Sutton, M. A., Erisman, J. W., Kruit, R. W., Zanten, M. van, Whitburn, S.,
655 Hadji-Lazaro, J., Hurtmans, D., Clerbaux, C., and Coheur, P.-F.: Global, regional and national trends of atmospheric
656 ammonia derived from a decadal (2008–2018) satellite record, Environ. Res. Lett., 16, 055017,
657 https://doi.org/10.1088/1748-9326/abd5e0, 2021.

658 Vira, J., Hess, P., Ossohou, M., and Galy-Lacaux, C.: Evaluation of interactive and prescribed agricultural ammonia
659 emissions for simulating atmospheric composition in CAM-chem, Atmospheric Chemistry and Physics, 22, 1883–
660 1904, https://doi.org/10.5194/acp-22-1883-2022, 2022.

661 Wang, R., Guo, X., Pan, D., Kelly, J. T., Bash, J. O., Sun, K., Paulot, F., Clarisse, L., Van Damme, M., Whitburn, S.,
662 Coheur, P.-F., Clerbaux, C., and Zondlo, M. A.: Monthly Patterns of Ammonia Over the Contiguous United States at
663 2-km Resolution, Geophysical Research Letters, 48, e2020GL090579, https://doi.org/10.1029/2020GL090579,
664 2021.

665 Wang, R., Pan, D., Guo, X., Sun, K., Clarisse, L., Van Damme, M., Coheur, P.-F., Clerbaux, C., Puchalski, M., and
666 Zondlo, M. A.: Bridging the spatial gaps of the Ammonia Monitoring Network using satellite ammonia
667 measurements, Atmospheric Chemistry and Physics, 23, 13217–13234, https://doi.org/10.5194/acp-23-13217-2023,
668 2023.

669   Warner, J. X., Wei, Z., Strow, L. L., Dickerson, R. R., and Nowak, J. B.: The global tropospheric ammonia
670   distribution as seen in the 13-year AIRS measurement record, Atmospheric Chemistry and Physics, 16, 5467–5479,
671   https://doi.org/10.5194/acp-16-5467-2016, 2016.

672   Wright, R., Lucey, P., Flynn, L., Ferrari-Wong, C., Gabrieli, A., Nunes, M., Gunapala, S., Ting, D., Rafol, S., Soibel,
673   A., and George, T.: HYTI: High Spectral and Spatial Resolution Thermal Imaging from a 6U CubeSat, Small
674   Satellite Conference, 2020.

675   Wyer, K. E., Kelleghan, D. B., Blanes-Vidal, V., Schauberger, G., and Curran, T. P.: Ammonia emissions from
676   agriculture and their contribution to fine particulate matter: A review of implications for human health, Journal of
677   Environmental Management, 323, 116285, https://doi.org/10.1016/j.jenvman.2022.116285, 2022a.

678   Wyer, K. E., Kelleghan, D. B., Blanes-Vidal, V., Schauberger, G., and Curran, T. P.: Ammonia emissions from
679   agriculture and their contribution to fine particulate matter: A review of implications for human health, Journal of
680   Environmental Management, 323, 116285, https://doi.org/10.1016/j.jenvman.2022.116285, 2022b.

681   Yu, F., Nair, A. A., and Luo, G.: Long-Term Trend of Gaseous Ammonia Over the United States: Modeling and
682   Comparison With Observations, Journal of Geophysical Research: Atmospheres, 123, 8315–8325,
683   https://doi.org/10.1029/2018JD028412, 2018.

684   Zeng, Y., Tian, S., and Pan, Y.: Revealing the Sources of Atmospheric Ammonia: a Review, Curr Pollution Rep, 4,
685   189–197, https://doi.org/10.1007/s40726-018-0096-6, 2018.

686   Zhang, L., Jacob, D. J., Knipping, E. M., Kumar, N., Munger, J. W., Carouge, C. C., van Donkelaar, A., Wang, Y. X.,
687   and Chen, D.: Nitrogen deposition to the United States: distribution, sources, and processes, Atmospheric Chemistry
688   and Physics, 12, 4539–4554, https://doi.org/10.5194/acp-12-4539-2012, 2012.

689